Nano Research

Open Access

Research Article

Initiator quenching induced spatial regulation of *in-situ* gelation enables gradient gel-liquid electrolyte for durable Zn-metal batteries

Yuanjie Zheng[1,§], Kai Du[1,§], Zhao Yue[1], Xinqi Huang[1], Chunyang Xu[1]✉, Liu Wang[1]✉, and Xinwei Cui[1,2]

[1] *Henan Institutes of Advanced Technology, Zhengzhou University, Zhengzhou 450003, China*
[2] *College of Materials Science and Engineering, Zhengzhou University, Zhengzhou 450001, China*
[§] *Yuanjie Zheng and Kai Du contributed equally to this work.*

Cite this article: *Nano Research*, **2026**, *19*, 94908516. https://doi.org/10.26599/NR.2026.94908516

ABSTRACT: Gel electrolytes represent a promising alternative to liquid counterparts for mitigating free water-induced parasitic reactions at Zn metal anodes. However, the intrinsically sluggish ion transport within homogeneous gel networks severely impedes electrochemical kinetics. Herein, a novel gradient gel-liquid electrolyte (G-PAM) is proposed to reconcile interfacial stability with rapid ion transport. By introducing a Mn^{2+}-rich coating on the cathode-facing side of the separator to locally quench persulfate initiators and inhibit polymerization, precise spatial control over the *in-situ* gelation of acrylamide monomers is realized, enabling selective gel formation at the anode side while preserving a liquid phase near the cathode. This functional graded electrolyte exhibits high ionic conductivity (2.52 × 10^{-2} S·cm^{-1}) comparable to liquid electrolyte, ensuring fast charge transfer kinetics. Moreover, the amide-induced solvation restructuring favors the formation of a thin, stable N-rich solid electrolyte interphase (SEI), which enhances anodic interfacial stability and facilitates uniform Zn deposition. Consequently, ultra-stable Zn plating/stripping over 11,000 h is achieved. Zn||MnO_2 full cells exhibit excellent rate performance and long-term cycling stability with minimal capacity decay of only 0.011% per cycle. This *in-situ* spatial regulation strategy establishes a new paradigm for designing functionally graded electrolytes, paving the way toward practical, high-performance Zn-based batteries.

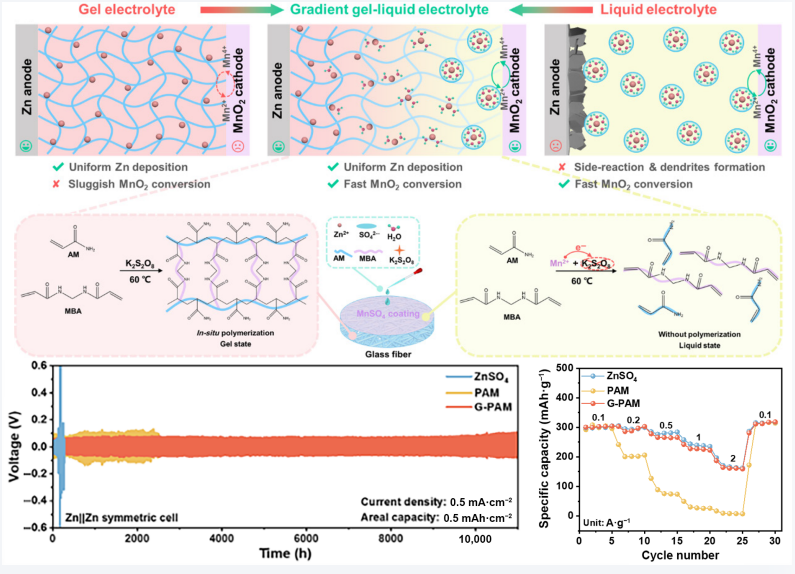

KEYWORDS: *in-situ* gelation, gradient gel-liquid electrolytes, Zn-metal batteries, interfacial stability, reaction kinetics

1 Introduction

Rechargeable aqueous Zn-based batteries have long been regarded as a promising candidate for wearable electronic and stationary energy storage due to their high energy density, intrinsic safety, resource abundance, and environmental benignity [1, 2]. These merits primarily stem from the utilization of Zn metal as anode, which features a moderate redox potential (−0.76 V vs. standard hydrogen electrode (SHE)) and ultrahigh volumetric capacity (5855 mAh·cm^{-3}) [3, 4]. However, the poor reversibility of Zn metal anode, originating from hydrogen evolution reactions (HER), parasitic side reactions, and dendrite formation, severely deteriorates their energy efficiency and cycling lifespan [5, 6]. As a result, most commercial Zn-based batteries (such as alkaline Zn–MnO_2 and Zn–Ag_2O systems) remain limited as non-rechargeable primary cells [7, 8]. To overcome these challenges, extensive efforts have been devoted through strategies, including three-dimensional (3D) structural design [9, 10], functional

Received: October 14, 2025; **Revised:** January 5, 2026
Accepted: January 31, 2026

✉Address correspondence to Chunyang Xu, chunyangxu@zzu.edu.cn; Liu Wang, wangliu@zzu.edu.cn

protective coatings [11, 12], electrolyte engineering [13, 14], and separator modification [15, 16]. Recent theoretical and experimental studies have highlighted that regulating Zn^{2+} migration dynamics and interfacial solvation structures is crucial for achieving rapid and uniform Zn deposition [17–19]. Among them, replacing the conventional liquid electrolyte with gel electrolytes provides a fundamental approach, which can mitigate water activity and simultaneously enhance interfacial mechanical robustness via immobilizing water molecules on polymer backbones [20–22], while enabling further regulation of interfacial Zn^{2+} transport and deposition behavior [23, 24]. These systems effectively suppress water-induced HER or other side reactions and enable high tolerance against dendrite penetration, thus improving the cycling stability of Zn metal anodes [25].

However, gel electrolytes generally suffer from severely limited ionic conductivity (σ) compared to their liquid counterparts, primarily due to the restrained mobility of solvent molecules. As a result, the reaction kinetics at electrode/electrolyte interface are significantly hampered, particularly under high-rate conditions [26, 27]. Additionally, the suppressed water activity in gel electrolytes impairs the proton-coupled cathode reactions (e.g., the Zn^{2+}/H^+ co-insertion process in MnO_2), thereby compromising their energy densities [28, 29]. These limitations indicate that a single homogeneous electrolyte faces intrinsic difficulty in simultaneously satisfying the distinct interfacial requirements, namely, suppressed interfacial side reactions at anode and fast reaction kinetics at cathode [30, 31]. To address this dilemma, spatially asymmetric electrolyte designs, such as gradient architectures, are envisioned as a compelling concept. By enabling a gradual transition from a gel phase near the anode to a liquid phase at the cathode, as illustrated in Fig. 1(a), these architectures may have the potential to reconcile the conflicting requirements within a single system. However, the development of scalable and practical methods for constructing such gradient gel-liquid electrolytes (G-PAM) remains a significant challenge.

In-situ gelation of vinyl-containing monomers offers an attractive strategy for constructing gel or solid electrolytes from liquid precursors [32, 33]. As a decisive factor that determines the resulting physical state and ionic transport properties, polymerization degree is governed by parameters, such as monomer concentration, temperature, redox environment, and the presence of radical scavengers [34–37]. However, within the confined geometry of a cell configuration, spatial regulation over parameters like concentration or temperature is technically challenging. In contrast, locally introducing redox-active additives, which can quench radicals or initiators, provides a more feasible route for spatially regulating the polymerization process and preserving unpolymerized regions with higher fluidity [38, 39]. Inspired by this concept, a gradient electrolyte should be realized by locally incorporating appropriate redox-active species near the cathode to disrupt the monomer polymerization, featuring an asymmetric structure that integrates polymerized gel near anode with unpolymerized liquid near cathode. In particular, strongly oxidizing persulfates are commonly used to initiate the polymerization of vinyl-based monomers in aqueous environment. Accordingly, low-valent Mn^{2+} ions are rationally selected as the polymerization regulators for their potential to deactivate persulfate initiator through redox reactions. Moreover, the manganese ions near cathode can simultaneously suppress manganese dissolution from MnO_2, thereby improving the cycling stability of cathode [28, 40].

Herein, a G-PAM is developed via spatially controlled *in-situ* gelation of acrylamide (AM) monomers. A $MnSO_4$-rich coating is introduced to the cathode-facing side of the separator to regulate the polymerization gradient as illustrated in Fig. 1(b). In the presence of persulfate initiator, AM monomers polymerize preferentially near the Zn anode side, establishing a stable, protective N-rich solid electrolyte interphase (SEI) that suppresses parasitic side reactions and facilitates uniform Zn deposition. Simultaneously, the Mn^{2+} ions at the cathode side quench the persulfate initiator, preventing local polymerization and preserving a fluidic liquid phase that favors ionic transport and efficient MnO_2 conversion kinetics. The resulting gradient gel-liquid electrolyte enables highly reversible Zn plating/stripping for over 11,000 h, while simultaneously delivering excellent rate capability and cycling stability in full cells.

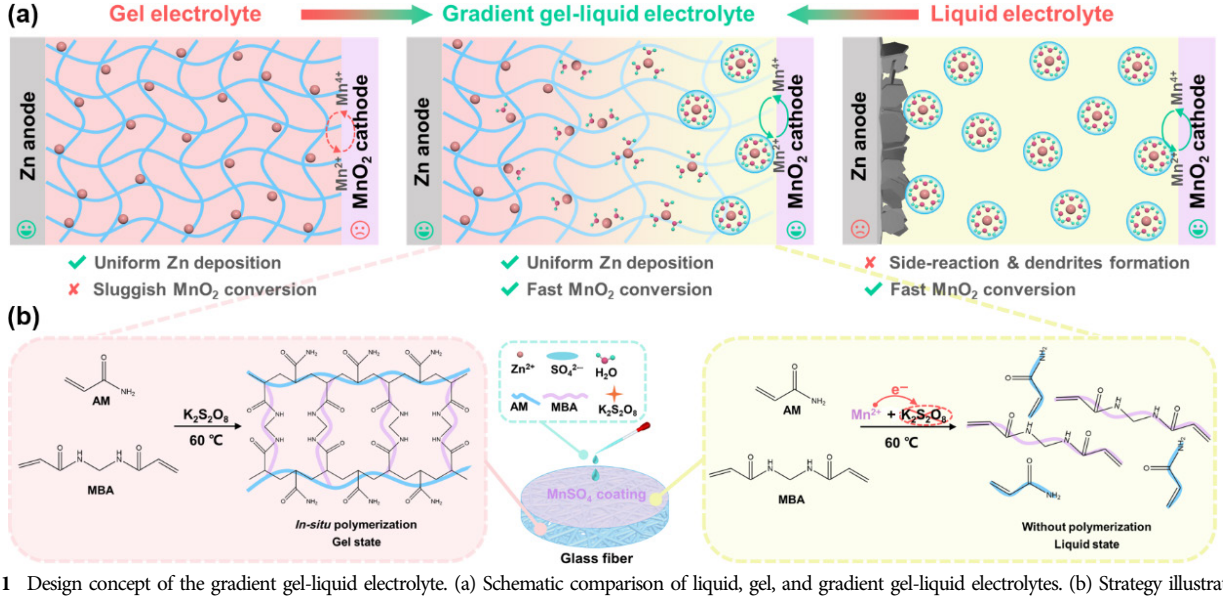

Figure 1 Design concept of the gradient gel-liquid electrolyte. (a) Schematic comparison of liquid, gel, and gradient gel-liquid electrolytes. (b) Strategy illustration for controlling the polymerization gradient.

2 Experimental section

2.1 Fabrication of gradient G-PAM electrolyte

A $MnSO_4$-coated glass fiber (GF) separator was first fabricated. Typically, 0.169 g $MnSO_4·H_2O$ (99%, Aladdin) and 0.02 g carboxymethyl cellulose (CMC, Tianjin EVS) were dissolved in 2 mL deionized water under vigorous stirring. Then, 0.1 mL of the resulting slurry was uniformly blade-coated onto one side of a GF separator (GF/D, Whatman) with diameter of 16 mm, followed by drying at 60 °C for 10 h.

The precursor solution for *in-situ* gelation was prepared by dissolving 0.182 g AM (99%, Aladdin), 14 μL of aqueous N,N'-methylenebis(acrylamide) (MBA, 99%, Aladdin, 10 mg·mL^{-1}), and 23 μL of aqueous potassium persulfate (KPS, $K_2S_2O_8$, 99.5%, Aladdin, 20 mg·mL^{-1}) in 1 mL of 3 M $ZnSO_4$ solution. To fabricate the gradient G-PAM electrolyte, 180 μL of the precursor solution was dropped onto the $MnSO_4$-coated GF separator, followed by heating at 60 °C for 60 min to initiate the polymerization.

2.2 Synthesis of MnO_2 cathode

For MnO_2 synthesis, 0.459 g $MnSO_4·H_2O$ and 2 mL of 0.5 M H_2SO_4 were dissolved in 90 mL of deionized water under magnetic stirring. Then, 20 mL of 0.1 M $KMnO_4$ solution was slowly added dropwise. The mixture was stirred at room temperature for 2 h, then transferred to a Teflon-lined autoclave, and heated at 120 °C for 12 h. After cooling, the precipitate was collected by centrifugation, washed three times with deionized water, and dried under vacuum at 60 °C for 12 h. To prepare the MnO_2 cathode, a slurry containing MnO_2, Super P (Timcal), and polyvinylidene fluoride (PVDF, analytical reagent (AR), Macklin) in a mass ratio of 8:1:1 was dispersed in N-methyl-2-pyrrolidone (NMP, 99%, Aladdin) and then coated on titanium foil (99.99%, Tianjin EVS). The electrodes were vacuum dried at 80 °C for 12 h. The typical MnO_2 mass loading was ~ 1.8 mg·cm^{-2}.

2.3 Cell assembly

CR2032-type coin cells were assembled for both Zn||Zn symmetric cells and Zn||MnO_2 full cells. Zn plate with thickness of 100 μm was used as anode without further treatment. During cell assembly for the gradient G-PAM electrolyte, 180 μL of the precursor solution was dropped onto the $MnSO_4$-coated GF separator, with the coated side facing the cathode. After sealing, the cells were heated at 60 °C for 60 min to induce *in-situ* gelation. Homogeneous gel electrolyte (PAM)-based cells were assembled similarly, except using bare GF separators without $MnSO_4$-coating. Liquid electrolyte-based cells used 3 M $ZnSO_4$ solution as the electrolyte. The thickness of the GF separator is 600 μm, which is equal to that of the electrolyte.

2.4 Materials characterization

X-ray diffraction (XRD, Bruker D8 Advance) was carried out to identify the crystalline phases of the cycled Zn anodes. Scanning electron microscopy (SEM, ZEISS Gemini 300) with energy-dispersive X-ray spectroscopy (EDS) was employed for morphology analysis. Polymerization behavior of the gradient electrolyte was investigated using *in-situ* Raman spectroscopy (LabRAM HR800) and Fourier transform infrared (FTIR) spectroscopy (Bruker Vertex 70). Ultraviolet–visible–near infrared spectroscopy (UV–Vis–NIR, Shimadzu UV-3600 Plus) was used to evaluate the KPS activity. X-ray photoelectron spectroscopy (XPS, Thermo ESCALAB 250Xi) etching measurements were conducted to analyze the interfacial chemistry on cycled Zn anodes. 3D surface profiles and roughness were characterized by laser confocal microscopy (LCM, KEYENCE VK-X150).

2.5 Computational methods

Quantum chemical calculations were performed using density functional theory (DFT) on the Gaussian 09 program at the B3LYP/6-31+G(d,p) level, evaluating the dipole moments of AM and H_2O, binding energies of AM–Zn^{2+} and H_2O–Zn^{2+}, frontier orbitals and electrostatic potential of $[Zn(H_2O)_5AM]^{2+}$ and $[Zn(H_2O)_5AM]^{2+}$ solvation structures. The visualization was conducted based on Multiwfn in combination with visual molecular dynamics (VMD) software [41, 42].

2.6 Electrochemical measurements

Galvanostatic charge–discharge (GCD) tests were conducted using NEWARE battery testing system. Zn||Zn symmetric cells were cycled at defined current densities and areal capacities. Zn||MnO_2 full cells were tested in the voltage range of 1.0–1.8 V at various current rates. Cyclic voltammetry (CV), linear sweep voltammetry (LSV), and electrochemical impedance spectroscopy (EIS) measurements were performed on a Biologic electrochemical workstation (VMP-3e). Tafel curves were derived from LSV measurements on Zn||Zn symmetric cells applying different electrolytes at potential range from −0.4 to 0.4 V with a scan rate of 1 mV·s^{-1}.

Ionic conductivities were measured via EIS on a symmetric configuration using stainless steel electrodes. The EIS was performed with a 10 mV amplitude sine wave from 1 MHz to 1 Hz. σ was calculated based on Eq. (1)

$$\sigma = \frac{L}{RS} \tag{1}$$

where L is the electrolyte thickness, R is the resistance obtained by EIS, and S is the electrode area.

The activation energy (E_a) was determined by measuring EIS on Zn||Zn symmetric cells at temperatures from 30 to 70 °C and linear fitting the charge transfer resistance according to Arrhenius relationship described by Eq. (2)

$$\frac{1}{R_{ct}} = A\exp\left(-\frac{E_a}{RT}\right) \tag{2}$$

3 Results and discussions

3.1 Characterization of the gradient structure

To validate the successful construction of the gradient gel-liquid electrolyte, the tunability of AM monomer polymerization was first evaluated. As visually demonstrated in the photographs (Fig. 2(a)), the aqueous $ZnSO_4$ solution containing AM as monomers, MBA as crosslinkers, and KPS as a thermal initiator, transformed into a solid hydrogel after curing at 60 °C for 60 min, confirming the successful polymerization. The dominant elastic response ($G' > G''$, where G' denotes the storage modulus and G'' denotes the loss modulus) and high tensile deformability of the gel (Fig. S1 in the Electronic Supplementary Material (ESM)) indicate a sufficient mechanical compliance and integrity to buffer interfacial stress and stabilize the Zn anode during repeated plating/stripping. In

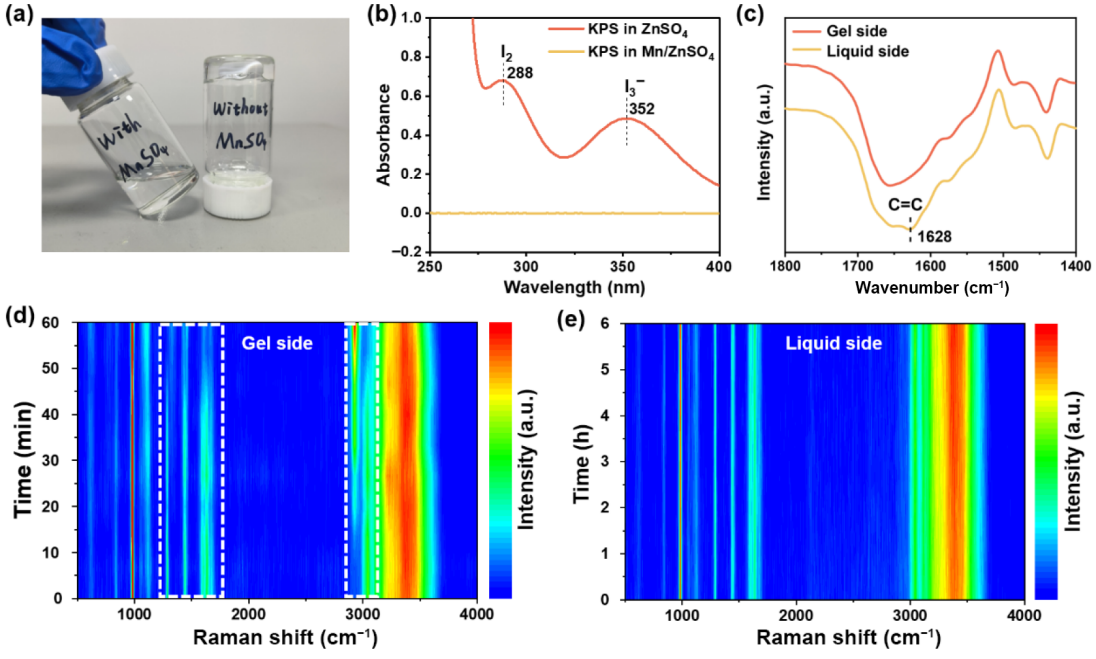

Figure 2 Characterization of the gradient architecture. (a) Digital photographs of the AM precursor after thermal treatment with and without $MnSO_4$. (b) UV–Vis–NIR spectra of KI oxidation by KPS with and without $MnSO_4$. (c) FTIR spectra of the gradient electrolyte collected from the gel side and liquid side. ((d) and (e)) *In-situ* Raman spectra of the gradient electrolyte at (d) gel side and (e) liquid side.

contrast, introducing $MnSO_4$ into the same precursor resulted in a persistent fluid liquid state under identical thermal curing conditions, suggesting that polymerization was effectively inhibited in the presence of Mn^{2+}. To clarify the role of Mn^{2+} in modulating the polymerization process, a potassium iodide (KI) catalytic probe experiment was performed to assess the oxidative activity of KPS [43, 44]. As shown in the UV–Vis–NIR spectra (Fig. 2(b)), characteristic absorption peaks at 288 and 352 nm, corresponding to I_2 and I_3^- as the oxidation products of KI, are clearly observed in the $ZnSO_4$ solution, confirming that the persulfate initiator remains active. In contrast, these peaks are absent in the $MnSO_4$-containing solution, indicating the deactivation of persulfate initiator. The direct chemical reaction between Mn^{2+} and KPS was further confirmed by UV–Vis, XRD, and FTIR analyses (Figs. S2–S4 in the ESM), resulting in the formation of MnO_2 species and the decomposition of peroxydisulfate. These results manifest that Mn^{2+} consumes the initiator via redox reaction, thereby enabling the unpolymerized AM.

The presence of a polymerization gradient within the thermal-cured electrolyte was confirmed by FTIR spectroscopy on both the gel and liquid sides. As shown in Fig. 2(c), the liquid side exhibits a C=C stretching vibration at 1628 cm^{-1}, characteristic of unpolymerized AM monomers. While this signal is significantly diminished on the gel side, it confirms the successful polymerization and formation of an asymmetric gel-liquid structure. The pronounced cross-sectional morphological evolution observed in SEM images (Fig. S5 in the ESM), together with the gradual attenuation of vinyl-associated vibrations and the enhancement of alkyl-related signals in the Raman line-scan (Fig. S6 in the ESM) from the liquid side to the gel side, further confirms the gel-liquid gradient structure. EDS analysis reveals that Mn is primarily confined to the liquid side of the electrolyte, with negligible Mn detected in the gel side or on the Zn anode after cycling (Figs. S7–S11 in the ESM). *In-situ* Raman spectroscopy further tracked the polymerization process during thermal curing treatment. As exhibited in Fig. 2(d), on the $MnSO_4$-free side, a new peak at 2929 cm^{-1} appears after 10 min of curing and progressively intensifies over time, which is assigned to alkyl C–H symmetric stretching vibration [45]. Concurrently, characteristic peaks at 3043 and 3116 cm^{-1}, associated with vinyl C–H stretching and vinyl CH_2 asymmetric stretching, respectively, gradually diminish and completely disappear by 45 min. Additionally, signals at 1289, 1440, and 1638 cm^{-1} corresponding to C–H bending, CH_2 bending, and C=C stretching also exhibit a pronounced decline in intensity. These spectral evolutions, marked by the emergence of alkyl-related signals and the concurrent disappearance of vinyl-associated vibrations, collectively indicate the progressive consumption of vinyl groups in AM monomers and the *in-situ* formation of poly(acrylamide) (PAM) chains during the thermal curing process within 60 min [46]. In stark contrast, the Raman spectra from the $MnSO_4$-coated side (Fig. 2(e)) show negligible changes, even after 6 h of thermal treatment. The vinyl-related signals persist, and no noticeable alkyl-related peak is observed at around 2929 cm^{-1}, confirming the suppressed polymerization and the preservation of liquid phase in the Mn^{2+}-rich region. Final-state of the Raman spectra in Fig. S12 in the ESM further highlight the significant contrast between the polymerized and unpolymerized regions. These findings collectively confirm the tunable nature of AM polymerization under the regulation of Mn^{2+}, enabling precise spatial control and successful construction of a well-defined gel-liquid gradient structure within the electrolyte.

3.2 Anodic interfacial stability of the G-PAM electrolyte

To evaluate the capability of the gradient electrolyte for providing sufficient ionic transport to support efficient electrochemical reactions, the ionic conductivities of three representative electrolytes were measured. As shown in Fig. 3(a), the liquid $ZnSO_4$ electrolyte exhibits the highest ionic conductivity of 4.80×10^{-2} S·cm^{-1}, owing

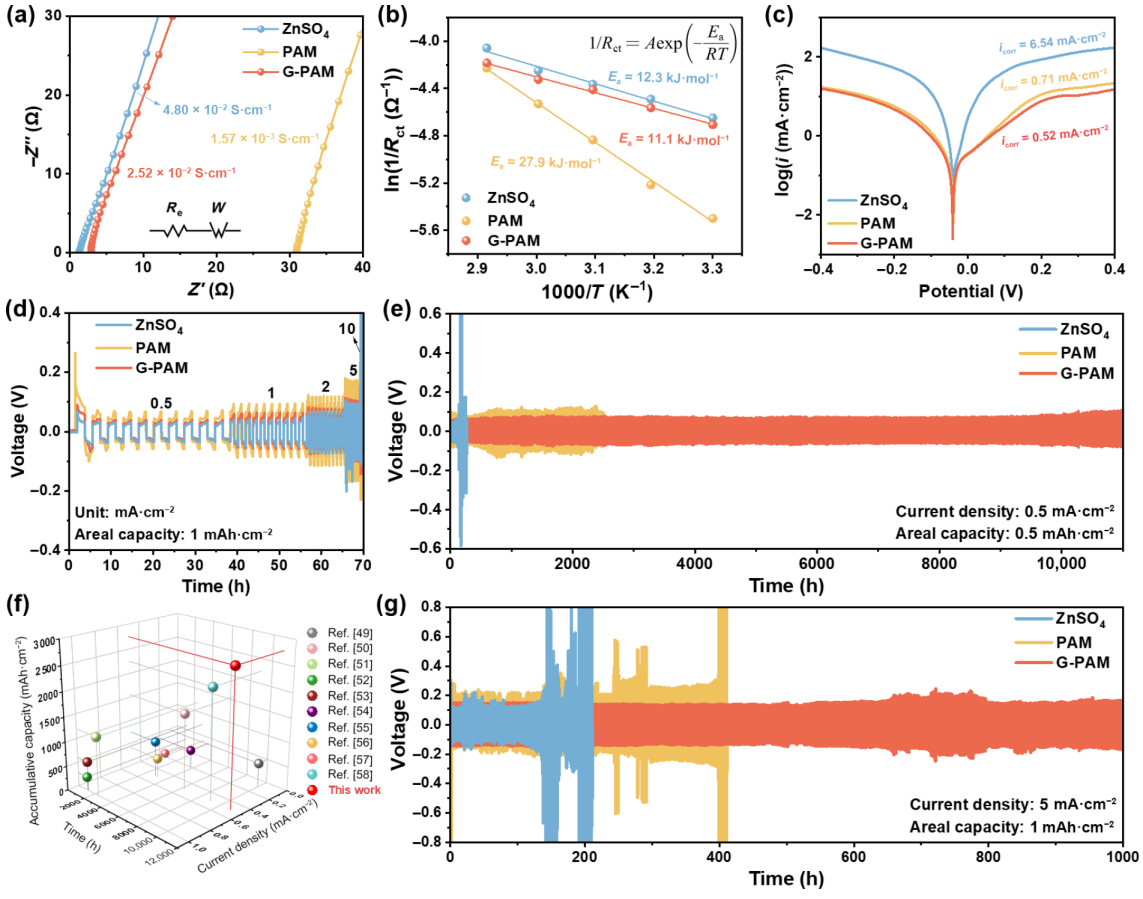

Figure 3 Anodic interfacial stability of the three electrolytes: Liquid $ZnSO_4$, gel PAM, and gradient G-PAM. (a) Ionic conductivities (equivalent circuit in the inset), (b) activation energies, and (c) Tafel curves of the three electrolytes. (d) Rate performance of Zn||Zn symmetric cells. (e) Long-term cycling profiles of Zn||Zn symmetric cells at 0.5 mA·cm^{-2} for 0.5 mAh·cm^{-2}. (f) Comparison of Zn plating/stripping cycling for G-PAM with recently reported gel electrolytes. (g) Long-term cycling profiles at 5 mA·cm^{-2} for 1 mAh·cm^{-2}.

to the free mobility of solvated Zn^{2+} ions in the unconfined aqueous environment. In stark contrast, the homogeneous gel electrolyte (referred to as PAM) displays a significantly lower ionic conductivity of only 1.57×10^{-3} S·cm^{-1}, as the mobility of water molecules and solvated ions is greatly restricted by the polymeric network anchoring. Remarkably, the G-PAM gradient electrolyte delivers an intermediate yet sufficiently high ionic conductivity of 2.52×10^{-2} S·cm^{-1}, approaching that of the liquid electrolyte and exceeding the homogeneous gel electrolyte by more than an order of magnitude. Additionally, the G-PAM electrolyte exhibits a relatively high Zn^{2+} diffusion coefficient (9.89×10^{-7} cm^2·s^{-1}) comparable to that of liquid electrolyte and significantly higher than that of the PAM electrolyte (Fig. S13 in the ESM), which is favorable for alleviating concentration polarization during prolonged cycling. These results confirm that the gradient structure successfully balances polymer rigidity with ionic transport, ensuring fast ion migration essential for sustaining rapid electrochemical reactions. The interfacial Zn^{2+} transfer kinetics were further evaluated by analyzing the E_a via temperature-dependent EIS measurements on Zn||Zn symmetric cells. As shown in Fig. 3(b) and Fig. S14 in the ESM, the gradient G-PAM electrolyte exhibits a significantly reduced E_a of 11.1 kJ·mol^{-1} compared with 27.9 kJ·mol^{-1} for the homogeneous gel PAM electrolyte, reflecting its enhanced ion migration rate and improved interfacial ion transfer kinetics [47, 48]. Notably, the E_a of G-PAM is even slightly lower than that of liquid $ZnSO_4$ electrolytes (12.3 kJ·mol^{-1}), despite their comparable ionic conductivities. This result suggests that, beyond the enhanced ionic migration rate, the gradient structure promotes more homogeneous interfacial ion distribution and faster interfacial ion transfer, potentially due to the formation of a favored SEI layer and suppression of side reactions that may otherwise deteriorate interfacial kinetics.

The corrosion behavior of the Zn anode in different electrolytes was further investigated via Tafel analysis (Fig. 3(c)). The liquid $ZnSO_4$ electrolyte exhibits a high corrosion current density of 6.54 mA·cm^{-2}, indicative of pronounced parasitic reactions such as HER and Zn oxidation. In comparison, both the PAM-based gel electrolyte and the gradient G-PAM electrolyte significantly reduce the corrosion current. Particularly, the G-PAM electrolyte achieves a corrosion current density as low as 0.52 mA·cm^{-2}, suggesting the formation of a more passivated Zn/electrolyte interface that effectively suppresses the undesirable water-induced side reactions.

As a result of the enhanced interfacial charge transfer kinetics combined with the inhibited corrosion reactions, a favored Zn deposition behavior should be expected. To examine the reversibility of Zn plating and stripping, galvanostatic cycling tests were conducted using Zn||Zn symmetric cells. As shown in Fig. 3(d), the G-PAM electrolyte consistently delivers smooth and stable voltage profiles with low overpotentials across a wide range of current densities from 0.5 to 10 mA·cm^{-2}, indicating excellent interfacial compatibility and fast charge transfer kinetics. In contrast, the gel PAM electrolyte exhibits significantly larger

overpotentials at each current rate, a direct consequence of its limited ionic conductivity. While the liquid $ZnSO_4$ electrolyte exhibits lowest overpotentials under moderate current densities (< 5 mA·cm^{-2}), it experiences drastic voltage fluctuations and instability at 10 mA·cm^{-2}, as magnified in Fig. S15 in the ESM, implying unstable Zn deposition behavior and severe side reactions at high-rate conditions. Benefiting from the favorable ion transport characteristics and interfacial stability, the G-PAM electrolyte enables ultralong-term cycling with outstanding durability. As displayed in Fig. 3(e), the Zn||Zn symmetric cell achieves a lifespan exceeding 11,000 h at 0.5 mA·cm^{-2} with an areal capacity of 0.5 mAh·cm^{-2}, while maintaining a stable overpotential of approximately 70 mV throughout. In contrast, the liquid $ZnSO_4$ electrolyte fails catastrophically after only ~ 250 h, originating from the uncontrolled interfacial side reactions. The gel PAM electrolyte exhibits a persistently larger overpotential for ~ 2500 h before ultimately failing. *In-situ* EIS further indicates a stable Zn/electrolyte interface and more uniform interfacial Zn^{2+} transport in the G-PAM electrolyte during cycling (Fig. S16 in the ESM). As a comparative analysis shown in Fig. 3(f), the G-PAM electrolyte exhibits significantly superior long-term cycling stability over recent gel electrolytes, featuring extended cycle life and higher accumulative capacity under comparable current densities [49–58]. Furthermore, even under harsh conditions of high current density (5 mA·cm^{-2}) and high areal capacity (1 mAh·cm^{-2}), the G-PAM electrolyte maintains robust performance with a cycle life exceeding 1000 h and a steady voltage hysteresis of ~ 140 mV as presented in Fig. 3(g). The absence of soft shorting or intermittent drops in the zoomed-in voltage profiles further confirms the excellent interfacial stability enabled by the G-PAM electrolyte (Figs. S17 and S18 in the ESM). In contrast, both the liquid $ZnSO_4$ and PAM electrolytes encounter immediate voltage instabilities and fail rapidly after only 200 and 400 h, respectively. Even under harsher conditions at 10 mA·cm^{-2} with 5 mAh·cm^{-2}, the G-PAM electrolyte sustains stable cycles for more than 200 h (Fig. S19 in the ESM). Excellent interfacial adhesion is also observed (Fig. S20 in the ESM), which is beneficial for maintaining uniform ion transport and stable interfacial contact. Collectively, these results underscore the exceptional anodic interfacial stability and long-term Zn plating/stripping reversibility enabled by the gradient G-PAM electrolyte.

3.3 Zn deposition characterization and interfacial stabilization mechanism

A series of post-mortem characterizations was conducted on the cycled Zn metal anodes to evaluate the Zn deposition performance facilitated by the G-PAM electrolyte. As shown in Fig. 4(a), the Zn anode retrieved from the G-PAM cell after 100 cycles exhibits ultra-flat surface covered with curled morphologies that likely originate from residual PAM polymer. Elemental mapping reveals a uniform distribution of Zn, N, S, O, and C elements, confirming the homogeneous Zn deposition and the formation of an N-containing interphase. The N-containing interphase potentially acts as a protective barrier, mitigating corrosion from the liquid attack and effectively suppressing dendrite growth. In stark contrast, the Zn anode cycled in the liquid $ZnSO_4$ electrolyte presents a characteristic dendritic morphology covered with numerous flaky byproducts (Fig. 4(b)). Elemental mapping reveals highly concentrated regions of S and O, suggesting uneven Zn deposition accompanied by uncontrollable proliferation of alkaline sulfate byproducts. LCM was further conducted to evaluate the surface roughness of the cycled electrodes. As displayed in Fig. 4(c) and Fig. S21 in the ESM, the electrode cycled with G-PAM electrolyte retains a remarkably flat and smooth surface, with minimal variation of less than 3.08 μm in roughness (Fig. 4(d)). On the contrary, the electrode with liquid $ZnSO_4$ electrolyte exhibits pronounced surface protrusions and pits (Fig. 4(e)), with a significantly higher roughness of 69.92 μm (Fig. 4(f)), clearly indicating severe structural degradation.

XRD analysis further elucidates the crystal composition of the cycled Zn electrodes equipped with different electrolytes. As shown in Fig. 4(g), the Zn anode from G-PAM electrolyte exhibits sharp and intense diffraction peaks corresponding to metallic Zn, with negligible signals from $Zn_4SO_4(OH)_6{\cdot}5H_2O$ byproducts. This implies that parasitic reactions involving water molecules are effectively inhibited. In contrast, the electrode from liquid $ZnSO_4$ electrolyte shows dominant diffraction peaks from $Zn_4SO_4(OH)_6{\cdot}5H_2O$ (PDF#39-0688), alongside diminished metallic Zn peaks, indicating the presence of thick insulating byproduct layers that impede electrochemical performance.

To further probe the interfacial chemistry evolution of the cycled Zn anodes, XPS depth profiling analysis was conducted. As shown in Figs. 4(h)–4(o), both G-PAM and $ZnSO_4$ anodes exhibit Zn 2p signals corresponding to Zn^{2+} species at the surface (0 s), together with evident SO_4^{2-} signals in the O 1s and S 2p spectra, confirming the formation of a sulfate-containing surface layer on both electrodes [59, 60]. Notably, distinct N signals are detected exclusively on the G-PAM anode (Fig. 4(k) and Fig. S22 in the ESM), which can be deconvoluted into C–N and Zn–N components. This observation, consistent with the SEM results discussed above (Fig. 4(a)), reveals the formation of an N-rich SEI likely originating from the reduction of amide groups on PAM chains. With increasing etching depth, the Zn 2p peaks of G-PAM anode rapidly shift to lower binding energies corresponding to metallic Zn, accompanied by the disappearance of SO_4^{2-} signals in O 1s and S 2p spectra. These pieces of evidence indicate a very thin interphase layer and effectively suppress side reactions. In stark contrast, the Zn anode from liquid $ZnSO_4$ cell retains strong Zn^{2+} signals and persistent SO_4^{2-} species even after 400 s of etching, suggesting the formation of a much thicker byproduct layer. The elemental content ratio in Fig. S22 in the ESM further corroborates this result. After 200 s of etching, the G-PAM electrode surface is dominated by Zn with trace O and no detectable S, while the $ZnSO_4$ electrode maintains high contents of O and S. These results demonstrate that the G-PAM electrolyte facilitates the formation of a thin, stable, N-rich SEI that protects the Zn surface from parasitic reactions and promotes uniform Zn deposition.

To gain deeper insight into the suppression of water-induced side reactions and the origin of the N-rich SEI layer, DFT calculations were conducted on the Zn^{2+} solvation structures. As displayed in Fig. 5(a), the AM monomer features a higher dipole moment (3.84 Debye (D)) than H_2O molecule (2.38 D), indicating its stronger solvation ability to coordinate and dissociate Zn^{2+} from SO_4^{2-} [61]. Correspondingly, the binding energies of Zn^{2+} with AM (−7.91, −7.83, and −6.80 eV for different coordinated configurations) are stronger than that with H_2O (−5.92 eV), as shown in Fig. 5(b), indicating that AM can partially replace H_2O in the primary solvation sheath to form a more stable $[Zn(H_2O)_5AM]^{2+}$ complex [50]. The lower electrostatic potential of this mixed solvation cluster compared with $[Zn(H_2O)_6]^{2+}$ (Fig. 5(c)) further confirms the charge shielding effect, consistent with the weakened

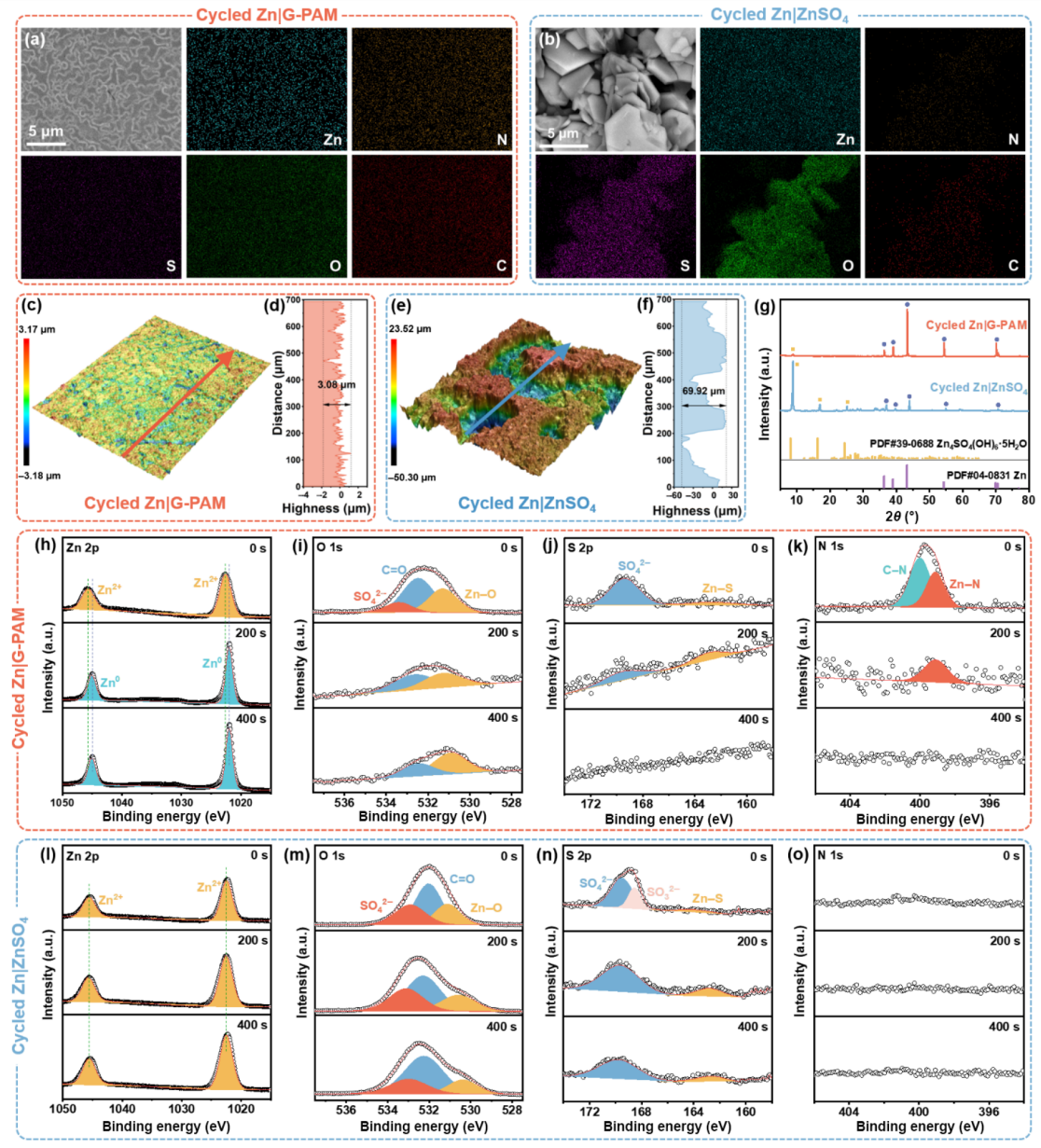

Figure 4 Post-mortem characterization of Zn anodes. ((a) and (b)) SEM images and EDS mapping of cycled Zn anodes with (a) G-PAM and (b) liquid $ZnSO_4$ electrolytes. ((c)–(f)) 3D laser confocal microscopy images and roughness profiles of cycled Zn with ((c) and (d)) G-PAM and ((e) and (f)) liquid $ZnSO_4$ electrolytes. (g) XRD patterns of Zn anodes after cycling in different electrolytes. ((h)–(o)) XPS depth profiles of Zn 2p, O 1s, S 2p, and N 1s from cycled Zn anodes with ((h)–(k)) G-PAM and ((l)–(o)) liquid $ZnSO_4$ electrolytes.

H_2O–Zn^{2+} interactions. Frontier orbital analysis (Fig. 5(d)) reveals that $[Zn(H_2O)_5AM]^{2+}$ possesses a higher lowest unoccupied molecular orbital (LUMO) energy level (−7.87 eV) than $[Zn(H_2O)_6]^{2+}$ (−8.43 eV), indicating its enhanced reductive stability [62]. Moreover, its LUMO distribution is mainly localized on the AM molecule rather than on H_2O, suggesting that AM moieties act as the preferential electron-accepting sites. Consequently, AM is reduced prior to H_2O, leading to the formation of an N-rich SEI layer [63], as evidenced by the XPS results (Fig. 4(k) and Fig. S5 in the ESM). This preferential reduction pathway simultaneously suppresses the activity of H_2O, thereby mitigating HER and the formation of water-derived byproducts.

Based on the combined experimental evidence and theoretical analysis, the anodic interfacial stabilization mechanism of the G-PAM electrolyte is illustrated in Fig. 5(e). (1) The strong coordination between amide groups on PAM and Zn^{2+} weakens Zn^{2+}–H_2O interactions, allowing partial substitution of H_2O in $[Zn(H_2O)_6]^{2+}$ and forming a more stable AM induced solvation structure; (2) The reduced activity of H_2O effectively suppresses HER and other water-induced parasitic reactions; (3) AM molecules undergo preferential reduction over H_2O, generating a robust N-rich SEI layer that promotes uniform nucleation and smooth Zn deposition.

3.4 Electrochemical performance of Zn||MnO_2 full cells

Building on the enhanced anodic interfacial stability and accelerated Zn^{2+} migration kinetics enabled by the gradient gel-liquid configuration, Zn||MnO_2 full cells employing a nanostructured

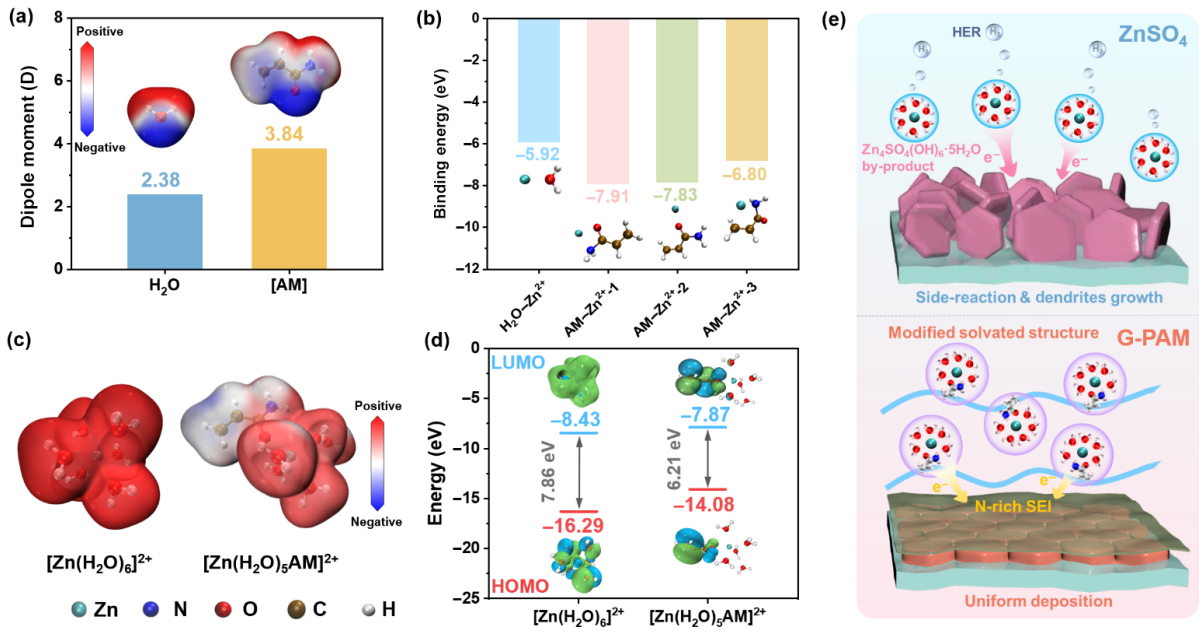

Figure 5 Theoretical investigation of the enhanced anodic interfacial stability enabled by G-PAM electrolyte. (a) Dipole moment values and electrostatic potential mappings (in the inset) of H_2O and AM monomer. (b) Binding energies of Zn^{2+} ion with H_2O and AM. (c) Electrostatic potential mappings and (d) highest occupied molecular orbital (HOMO) and lowest unoccupied molecular orbital (LUMO) energy levels of $[Zn(H_2O)_6]^{2+}$ and $[Zn(H_2O)_5AM]^{2+}$ solvation structures. (e) Schematic comparison of Zn plating behavior with $ZnSO_4$ and G-PAM electrolytes.

MnO_2 cathode with well-defined crystallinity (Figs. S23 and S24 in the ESM) were assembled to evaluate their practical applicability and overall electrochemical performance (Fig. 6(a)). CV tests were conducted using different electrolytes to probe their electrochemical redox reactions. As illustrated in Fig. 6(b), all three cells present CV curves with similar shapes, characteristic of the two-step redox reactions of MnO_2 cathode. Notably, compared with the G-PAM and $ZnSO_4$ cells, the PAM cell shows an obvious negative shift in cathodic peaks and a distinct positive shift in anodic peaks, indicating a larger polarization. This behavior reflects sluggish ion transport in the homogeneous gel PAM electrolyte, as previously discussed (Figs. 3(a) and 3(b)). In contrast, the G-PAM and $ZnSO_4$ cells possess almost overlapping redox peaks, demonstrating that the gradient electrolyte offers comparable electrochemical kinetics of the MnO_2 conversion, despite its partial gel state. In addition, the higher H^+-related capacity of G-PAM (Fig. S25 in the ESM) together with the larger area of cathodic peak at ~ 1.4 V, indicates a more favorable proton-involved redox process compared to the PAM electrolyte. As a result of the excellent reaction kinetics, the G-PAM based full cell exhibits outstanding rate performance comparable to that of the $ZnSO_4$ cell. As displayed in Figs. 6(c) and 6(d), the G-PAM cell delivers high specific capacities of 228 mAh·g^{-1} at 1 A·g^{-1} and 164 mAh·g^{-1} at 2 A·g^{-1}. In sharp contrast, the PAM-based cell suffers rapid capacity fading with increasing current density, retaining only 75 mAh·g^{-1} at 0.5 A·g^{-1}, which is primarily due to its poor Zn^{2+} transport across the cathode/electrolyte interface. Moreover, the G-PAM full cell exhibits remarkable long-term cycling stability (Fig. 6(e)), outperforming both the liquid and homogeneous gel electrolyte systems. It maintains a high capacity of 246 mAh·g^{-1} with 95.5% retention after 400 cycles at 0.5 A·g^{-1}, resulting in a remarkably lower decay rate of 0.011% per cycle compared to recently reported gel electrolytes (Fig. S26 in the ESM) [20, 31, 49–51, 53–58]. The durability is further supported by the nearly overlapping charge–discharge profiles throughout cycling (Fig. 6(f)), which reflects the highly reversible electrochemical reactions. Even at a high current density of 8 A·g^{-1}, the G-PAM cell delivers stable cycling for 1000 cycles (Fig. S27 in the ESM), indicating good durability under high-rate operation. This outstanding stability is primarily attributed to the enhanced Zn plating/stripping stability facilitated by the protective gel interface on the anode side and the formation of a stable N-rich SEI. The residual Mn^{2+} in the cathode-facing side of the G-PAM electrolyte may also help suppress Mn dissolution from the MnO_2 cathode, thereby further contributing to cycling stability. In contrast, despite a comparable high initial capacity, the $ZnSO_4$ cell encounters rapid decline in capacity due to the inferior anodic interfacial stability, remaining only 42 mAh·g^{-1} after 200 cycles.

Self-discharge performance, a critical indicator of shelf-life durability and closely associated with anodic interface degradation, was further examined by measuring the Coulombic efficiency (CE) after resting the fully charged cell for 24 h. As the voltage profiles recorded in Fig. 6(g), the liquid $ZnSO_4$-based cell shows a sharp voltage drop and a lower CE of only 77.4% after resting, indicative of significant parasitic reactions and unstable interfacial chemistry. On the contrary, the G-PAM cell exhibits a much slower voltage decay and significantly improved CE to 97.7%, comparable to that of PAM cell (98.4%). Even after 168 h of resting, the G-PAM cell maintains a high CE of 83.4% (Fig. S28 in the ESM), demonstrating excellent long-term self-discharge behavior. This enhancement clearly confirms the role of the gel phase in mitigating self-discharge due to stabilized anode/electrolyte interface. To demonstrate the practical potential of the gradient gel-liquid electrolyte, a MnO_2|G-PAM|Zn pouch cell was fabricated. As shown in Fig. 6(h), it successfully powers a sign panel containing 35 light-emitting diode (LED) bulbs, highlighting the feasibility of the gradient G-PAM electrolyte for application in large-scale Zn-based batteries.

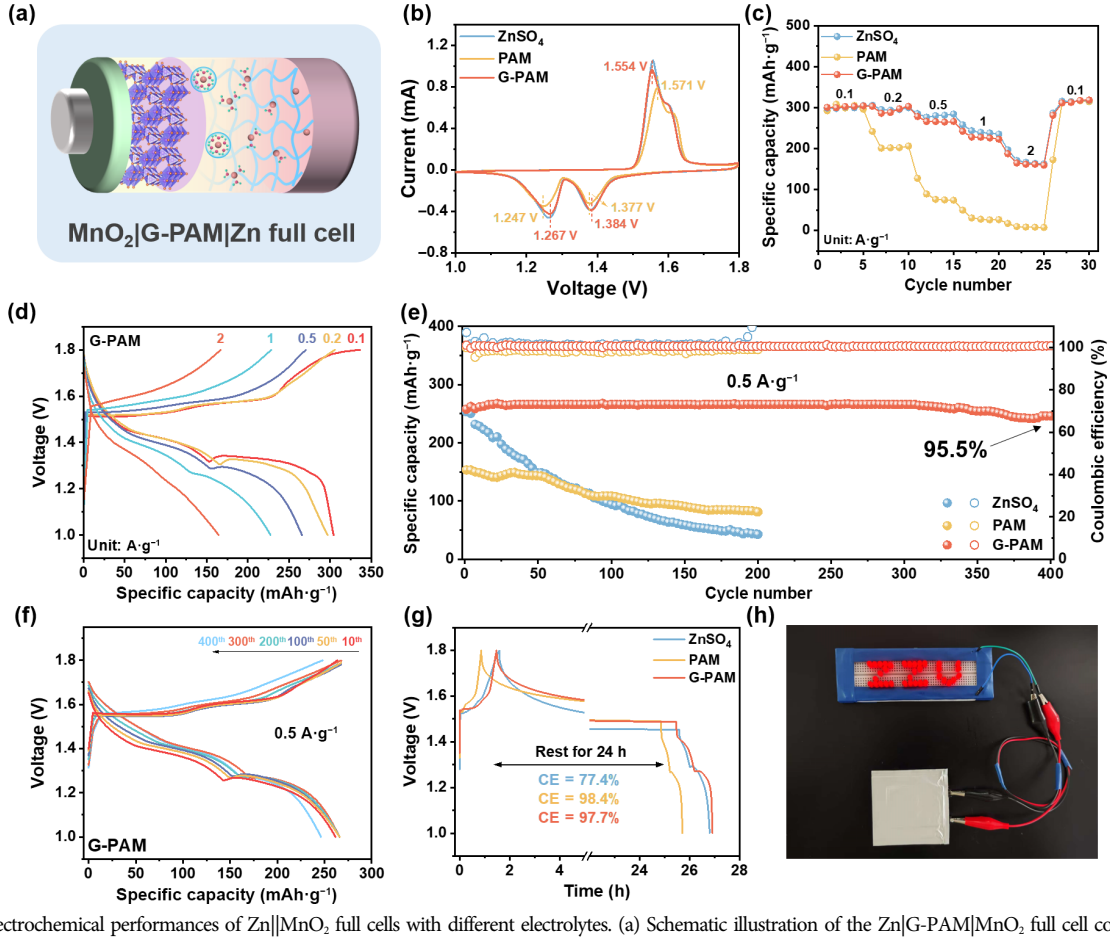

Figure 6 Electrochemical performances of Zn||MnO_2 full cells with different electrolytes. (a) Schematic illustration of the Zn|G-PAM|MnO_2 full cell configuration. (b) CV curves of Zn||MnO_2 full cells at 0.1 mV·s^{-1}. (c) Rate capacities and (d) corresponding charge–discharge profiles at current densities ranging from 0.1 to 2 A·g^{-1}. (e) Long-term cycling performance and (f) corresponding charge–discharge curves at 0.5 A·g^{-1}. (g) Self-discharge properties of Zn||MnO_2 full cells with different electrolytes. (h) Digital image of a G-PAM-based pouch cell powering an LED panel.

4 Conclusions

In summary, a functionally graded electrolyte (G-PAM) was developed to effectively reconcile the long-standing trade-off between interfacial stability and ionic transport in gel electrolyte for Zn metal batteries. This gradient gel-liquid architecture is realized by spatially regulating the *in-situ* gelation process of AM monomers, which is guided by a Mn^{2+}-rich coating on the cathode-facing side of separator. *In-situ* Raman spectroscopy directly tracked the polymerization process, verifying the successful formation of a polymerized gel phase at the Zn anode and an unpolymerized liquid phase at the cathode region. This unique configuration imparts high ionic conductivity (2.52×10^{-2} S·cm^{-1}) comparable to liquid electrolytes for fast electrochemical kinetics, and meanwhile forms a stable N-rich SEI layer that effectively mitigates water-induced parasitic reactions. As a result, the G-PAM electrolyte enables ultrastable Zn plating/stripping for over 11,000 h. In addition, it exhibits remarkable Zn||MnO_2 full cell performance with excellent rate capability (164 mAh·g^{-1} at 2 A·g^{-1}) and exceptionally low capacity decay of only 0.011% per cycle. This study demonstrates a scalable and practical strategy for electrolyte engineering that provides fresh insights into complex interface regulation, paving the way toward high-performance Zn-based batteries and other metal anode energy storage systems.

Electronic Supplementary Material: Supplementary material (Raman spectra, temperature-dependent EIS, voltage profiles of symmetric cells, LCM 2D images, comparison of cycling performance with recently reported gel electrolytes) is available in the online version of this article at https://doi.org/10.26599/NR.2026.94908516.

Data availability

All data needed to support the conclusions in the paper are presented in the manuscript and the Electronic Supplementary Material. Additional data related to this paper may be requested from the corresponding author upon request.

Acknowledgements

The authors gratefully acknowledge the financial support from the National Natural Science Foundation of China (Nos. 52403339 and 22508373), the Natural Science Foundation of Henan Province (No. 242300421426), and Fellowship of China Postdoctoral Science Foundation (No. 2023M743153).

Declaration of competing interest

All the contributing authors report no conflict of interests in this work.

Author contribution statement

Y. J. Z.: Investigation, methodology, data curation. K. D.: Investigation, data curation. Z. Y.: Data curation, formal analysis. X. Q. H.: Investigation, formal analysis. C. Y. X.: Supervision, writing – review & editing, project administration. L. W.: Conceptualization, writing – original draft, writing – review & editing, funding acquisition. X. W. C.: Project administration, resources. All the authors have approved the final manuscript.

Use of AI statement

None.

References

[1] Liang, Y. L.; Yao, Y. Designing modern aqueous batteries. *Nat. Rev. Mater.* **2023**, *8*, 109–122.

[2] Tang, L.; Peng, H. J.; Kang, J. R.; Chen, H.; Zhang, M. Y.; Liu, Y.; Kim, D. H.; Liu, Y. J.; Lin, Z. Q. Zn-based batteries for sustainable energy storage: Strategies and mechanisms. *Chem. Soc. Rev.* **2024**, *53*, 4877–4925.

[3] Liu, Y. Y.; Lu, X.; Lai, F. L.; Liu, T. X.; Shearing, P. R.; Parkin, I. P.; He, G. J.; Brett, D. J. L. Rechargeable aqueous Zn-based energy storage devices. *Joule* **2021**, *5*, 2845–2903.

[4] Kundu, D.; Adams, B. D.; Duffort, V.; Vajargah, S. H.; Nazar, L. F. A high-capacity and long-life aqueous rechargeable zinc battery using a metal oxide intercalation cathode. *Nat. Energy* **2016**, *1*, 16119.

[5] Lu, W. J.; Zhang, C. K.; Zhang, H. M.; Li, X. F. Anode for zinc-based batteries: Challenges, strategies, and prospects. *ACS Energy Lett.* **2021**, *6*, 2765–2785.

[6] Yang, Q.; Li, Q.; Liu, Z. X.; Wang, D. H.; Guo, Y.; Li, X. L.; Tang, Y. C.; Li, H. F.; Dong, B. B.; Zhi, C. Y. Dendrites in Zn-based batteries. *Adv. Mater.* **2020**, *32*, 2001854.

[7] Yan, H. B.; Li, S. M.; Zhong, J. Y.; Li, B. An electrochemical perspective of aqueous zinc metal anode. *Nanomicro Lett.* **2023**, *16*, 15.

[8] Zheng, J. X.; Deng, Y.; Yin, J. F.; Tang, T.; Garcia-Mendez, R.; Zhao, Q.; Archer, L. A. Textured electrodes: Manipulating built-in crystallographic heterogeneity of metal electrodes via severe plastic deformation. *Adv. Mater.* **2022**, *34*, 2106867.

[9] Mu, Y. B.; Li, Z.; Wu, B. K.; Huang, H. D.; Wu, F. H.; Chu, Y. Q.; Zou, L. F.; Yang, M.; He, J. F.; Ye, L. et al. 3D hierarchical graphene matrices enable stable Zn anodes for aqueous Zn batteries. *Nat. Commun.* **2023**, *14*, 4205.

[10] Zhang, G. H.; Zhang, X.; Liu, H. Z.; Li, J. H.; Chen, Y. Q.; Duan, H. G. 3D-printed multi-channel metal lattices enabling localized electric-field redistribution for dendrite-free aqueous Zn ion batteries. *Adv. Energy Mater.* **2021**, *11*, 2003927.

[11] Zheng, Z. Y.; Zhong, X. W.; Zhang, Q.; Zhang, M. T.; Dai, L. X.; Xiao, X.; Xu, J. H.; Jiao, M. L.; Wang, B. R.; Li, H. et al. An extended substrate screening strategy enabling a low lattice mismatch for highly reversible zinc anodes. *Nat. Commun.* **2024**, *15*, 753.

[12] Tian, X. M.; Zhao, Q.; Zhou, M. M.; Huang, X. J.; Sun, Y.; Duan, X. G.; Zhang, L.; Li, H.; Su, D. W.; Jia, B. H. et al. Synergy of dendrites-impeded atomic clusters dissociation and side reactions suppressed inert interface protection for ultrastable Zn anode. *Adv. Mater.* **2024**, *36*, 2400237.

[13] Shi, X.; Xie, J. H.; Wang, J.; Xie, S. L.; Yang, Z. J.; Lu, X. H. A weakly solvating electrolyte towards practical rechargeable aqueous zinc-ion batteries. *Nat. Commun.* **2024**, *15*, 302.

[14] Li, C. L.; Zhang, X. X.; Qu, G. M.; Zhao, S. S.; Qin, H. J.; Li, D. Z.; Li, N.; Wang, C. G.; Xu, X. J. Highly reversible Zn metal anode securing by functional electrolyte modulation. *Adv. Energy Mater.* **2024**, *14*, 2400872.

[15] Zhu, X. Q.; Xu, Z. M.; Zhang, T.; Zhang, J.; Guo, Y. F.; Shan, M. H.; Wang, K. H.; Shi, T. N.; Cui, G. S.; Wang, F. et al. Ultra-stable zinc anodes facilitated by hydrophilic polypropylene separators with large scale production capacity. *Adv. Funct. Mater.* **2024**, *34*, 2407262.

[16] Huang, X. Q.; Tian, Y. P.; Ma, X. K.; Zheng, Y. J.; Zhang, L.; Chao, Y. F.; Wang, L.; Cui, X. W. Promoting migration kinetic of desolvated Zn^{2+} by functional interlayer toward superior Zn metal anode. *Small* **2025**, *21*, 2500503.

[17] Guo, Y. M.; Wu, D. S.; Sun, Z.; Ning, F. H.; Zhu, K.; Liu, X. Y.; Lu, S. G.; Xia, Y. Y.; Yi, J. The role of ion-polaron electrostatic attraction on Zn^{2+} migration in α-V_2O_5 for zinc ion battery: Insights from first-principles calculations. *J. Phys. Chem. Lett.* **2025**, *16*, 1415–1423.

[18] Luo, B. Y.; Wang, H.; Chen, C.; Liu, L. C.; Wu, K.; Li, H. D.; Ye, D. F.; Li, Y. Y.; Cui, L.; Qiao, J. L. The zinc ion concentration dynamically regulated by an ionophore in the outer Helmholtz layer for stable Zn anode. *J. Colloid Interface Sci.* **2024**, *675*, 639–645.

[19] Zhang, H. Y.; Ning, F. H.; Guo, Y. M.; Subhan, S.; Liu, X. Y.; Shi, S. Q.; Lu, S. G.; Xia, Y. Y.; Yi, J. Unraveling the mechanisms of aqueous zinc ion batteries via first-principles calculations. *ACS Energy Lett.* **2024**, *9*, 4761–4784.

[20] Yang, S.; Wu, Q.; Li, Y.; Luo, F. S.; Zhang, J. L.; Chen, K.; You, Y.; Huang, J.; Xie, H. B.; Chen, Y. W. A Bio-inspired multifunctional hydrogel network with toughly interfacial chemistry for dendrite-free flexible zinc ion battery. *Angew. Chem., Int. Ed.* **2024**, *63*, e202409160.

[21] Lin, C. Y.; He, L. J.; Xiong, P. X.; Lin, H.; Lai, W. B.; Yang, X. H.; Xiao, F. Y.; Sun, X. L.; Qian, Q. R.; Liu, S. D. et al. Adaptive ionization-induced tunable electric double layer for practical Zn metal batteries over wide pH and temperature ranges. *ACS Nano* **2023**, *17*, 23181–23193.

[22] Yang, W. H.; Yang, Y.; Yang, H. J.; Zhou, H. S. Regulating water activity for rechargeable zinc-ion batteries: Progress and perspective. *ACS Energy Lett.* **2022**, *7*, 2515–2530.

[23] Zhan, S. K.; Liu, Z. X.; Ning, F. H.; Liu, X. Y.; Dai, Y.; Lu, S. G.; Xia, Y. Y.; Yi, J. Structure engineering by picosecond laser lithography boosts highly reversible Zn anode. *Adv. Funct. Mater.* **2025**, *35*, 2417546.

[24] Zhan, S. K.; Zhu, Y. H.; Li, Y. J.; Liu, X. Y.; Ning, F. H.; Xie, Y. H.; Lu, S. G.; Xia, Y. Y.; Yi, J. Magnetohydrodynamics and magnetic interface enable stable zinc anode. *Adv. Funct. Mater.* **2025**, *35*, 2507573.

[25] Liu, C. X.; Xie, X. S.; Lu, B.; Zhou, J.; Liang, S. Q. Electrolyte strategies toward better zinc-ion batteries. *ACS Energy Lett.* **2021**, *6*, 1015–1033.

[26] Wang, Y. B.; Li, Q.; Hong, H.; Yang, S.; Zhang, R.; Wang, X. Q.; Jin, X.; Xiong, B.; Bai, S. C.; Zhi, C. Y. Lean-water hydrogel electrolyte for zinc ion batteries. *Nat. Commun.* **2023**, *14*, 3890.

[27] Xie, J.; Liang, Z. J.; Lu, Y. C. Molecular crowding electrolytes for high-voltage aqueous batteries. *Nat. Mater.* **2020**, *19*, 1006–1011.

[28] Pan, H. L.; Shao, Y. Y.; Yan, P. F.; Cheng, Y. W.; Han, K. S.; Nie, Z. M.; Wang, C. M.; Yang, J. H.; Li, X. L.; Bhattacharya, P. et al. Reversible aqueous zinc/manganese oxide energy storage from conversion reactions. *Nat. Energy* **2016**, *1*, 16039.

[29] Zhang, N.; Chen, X. Y.; Yu, M.; Niu, Z. Q.; Cheng, F. Y.; Chen, J. Materials chemistry for rechargeable zinc-ion batteries. *Chem. Soc. Rev.* **2020**, *49*, 4203–4219.

[30] Chen, S. M.; Ying, Y. R.; Ma, L. T.; Zhu, D. M.; Huang, H. T.; Song, L.; Zhi, C. Y. An asymmetric electrolyte to simultaneously meet contradictory requirements of anode and cathode. *Nat. Commun.* **2023**, *14*, 2925.

[31] Zheng, L. H.; Chang, L. H.; Xue, S. Y.; Zhao, K. N.; Zhang, B. M.; He, W. D.; Tao, F.; Li, J. H.; Wang, M.; An, Q. Y. et al. Electrochemical responsive alginate chains rendered sol-to-gel gradient electrolyte towards practical Ah-level zinc metal pouch cell. *Angew. Chem., Int. Ed.* **2025**, *64*, e202502103.

[32] Zhang, S. H.; Xie, B.; Zhuang, X. C.; Wang, S. T.; Qiao, L. X.; Dong,

S. M.; Ma, J.; Zhou, Q.; Zhang, H. R.; Zhang, J. J. et al. Great challenges and new paradigm of the *in-situ* polymerization technology inside lithium batteries. *Adv. Funct. Mater.* **2024**, *34*, 2314063.
[33] Miao, X. Z.; Hong, J. H.; Huang, S.; Huang, C.; Liu, Y. S.; Liu, M.; Zhang, Q. Q.; Jin, H. Y. *In-situ* gel polymer electrolyte with rapid Li^+ transport channels and anchored anion sites for high-current-density lithium-ion batteries. *Adv. Funct. Mater.* **2025**, *35*, 2411751.
[34] Zou, S. H.; Yang, Y.; Wang, J. R.; Zhou, X. Y.; Wan, X. H.; Zhu, M.; Liu, J. *In-situ* polymerization of solid-state polymer electrolytes for lithium metal batteries: A review. *Energy Environ. Sci.* **2024**, *17*, 4426–4460.
[35] Li, P. Y.; Wang, S. Y.; Hao, J. J.; Wang, X.; Hao, S. M.; Lu, Y. H.; Li, H.; Zhou, W. D.; Li, Y. L. Efficiencies of various *in-situ* polymerizations of liquid electrolytes and the practical implications for quasi solid-state batteries. *Angew. Chem., Int. Ed.* **2023**, *62*, e202309613.
[36] Young, J. S.; Bowman, C. N. Effect of polymerization temperature and cross-linker concentration on reaction diffusion controlled termination. *Macromolecules* **1999**, *32*, 6073–6081.
[37] Tang, R. F.; Dong, H. F.; Lu, H. W.; Nie, J.; Zhu, X. Q. Customization of supramolecular hydrogels through one-step photopolymerization and its mechanism. *Chem. Mater.* **2023**, *35*, 4761–4771.
[38] Li, L.; Han, Q.; Wang, L.; Liu, B.; Wang, K. K.; Wang, Z. Y. Dual roles of MoS_2 nanosheets in advanced oxidation Processes: Activating permonosulfate and quenching radicals. *Chem. Eng. J.* **2022**, *440*, 135866.
[39] Jacky, P. E.; Easley, A. D.; Fors, B. P. Controlled anionic polymerization mediated by carbon dioxide. *Nat. Chem.* **2025**, *17*, 1076–1082.
[40] Lai, G. J.; Zhao, Z. Q.; Zhang, H.; Hu, X. T.; Lu, B.; Liang, S. Q.; Zhou, J. *In-situ* positive electrode–electrolyte interphase construction enables stable Ah-level Zn–MnO_2 batteries. *Nat. Commun.* **2025**, *16*, 2194.
[41] Lu, T. A comprehensive electron wavefunction analysis toolbox for chemists, Multiwfn. *J. Chem. Phys.* **2024**, *161*, 082503.
[42] Lu, T.; Chen, F. W. Multiwfn: A multifunctional wavefunction analyzer. *J. Comput. Chem.* **2012**, *33*, 580–592.
[43] Li, H.; Wang, N.; Lin, C. X.; Ren, Z. Q.; Du, Y. C.; Xu, Q. B,N dual-doped porous carbon nanoframeworks as bifunctional peroxymonosulfate activators for ultrafast adsorption and decomposition of microcontaminants in water. *Chem. Eng. J.* **2025**, *503*, 158349.
[44] Ali, J.; Lei, W. L.; Shahzad, A.; Ifthikar, J.; Aregay, G. G.; Shahib, I. I.; Elkhlifi, Z.; Chen, Z. L.; Chen, Z. Q. Regulating the redox centers of Fe through the enrichment of Mo moiety for persulfate activation: A new strategy to achieve maximum persulfate utilization efficiency. *Water Res.* **2020**, *181*, 115862.
[45] Zhang, X. C.; Li, D.; Yang, X. X.; Wang, L.; Li, G.; Wong, T. W.; Li, T. F.; Yang, W.; Luo, Z. S. Hydro-locking in hydrogel for extreme temperature tolerance. *Science* **2025**, *387*, 967–973.
[46] Qin, Y.; Li, H. F.; Han, C. P.; Mo, F. N.; Wang, X. Chemical welding of the electrode–electrolyte interface by Zn-metal-initiated *in-situ* gelation for ultralong-life Zn-ion batteries. *Adv. Mater.* **2022**, *34*, 2207118.
[47] Ma, H.; Yu, J. Q.; Chen, M. F.; Han, X.; Chen, J. Z.; Liu, B.; Shi, S. Q. Amino-enabled desolvation sieving effect realizes dendrite-inhibiting thin separator for durable aqueous zinc-ion batteries. *Adv. Funct. Mater.* **2023**, *33*, 2307384.
[48] Jiao, S. Q.; Fu, J. M.; Wu, M. Z.; Hua, T.; Hu, H. B. Ion sieve: Tailoring Zn^{2+} desolvation kinetics and flux toward dendrite-free metallic zinc anodes. *ACS Nano* **2022**, *16*, 1013–1024.
[49] Zheng, Q. Q.; Liu, L. Y.; Hu, Z. W.; Tang, Z. W.; Lu, H. Y.; Gao, Y. Q.; Wang, J. Y.; Song, Y. J.; Han, C.; Li, W. J. Altering the Zn^{2+} migration mechanism enables the composite hydrogel electrolytes with high Zn^{2+} conduction and superior anti-dehydration. *Adv. Funct. Mater.* **2025**, *35*, 2504782.
[50] An, Y. L.; Shu, C.; Liu, Y. Q.; Xu, Y. L.; Kang, L. T.; Zhang, X. Y.; Sun, J. C.; Ma, Z. J.; Zhao, K.; Huang, Y. F. et al. Modulating the hydrogen bond for a stable zinc anode with a wide temperature range via the sucrose and polyacrylamide synergistic effect. *ACS Nano* **2025**, *19*, 11146–11163.
[51] Cui, Y. L. S.; Chen, W. P.; Xin, W. W.; Ling, H. Y.; Hu, Y. H.; Zhang, Z. H.; He, X. F.; Zhao, Y.; Kong, X. Y.; Wen, L. P. et al. Gradient quasi-solid electrolyte enables selective and fast ion transport for robust aqueous zinc-ion batteries. *Adv. Mater.* **2024**, *36*, 2308639.
[52] Qiu, T. Y.; Wang, T. H.; Tang, W. S.; Li, Y. Q.; Li, Y. G.; Lang, X. Y.; Jiang, Q.; Tan, H. Q. Rapidly synthesized single-ion conductive hydrogel electrolyte for high-performance quasi-solid-state zinc-ion batteries. *Angew. Chem., Int. Ed.* **2023**, *62*, e202312020.
[53] Shi, M. Y.; Zhang, J. L.; Tang, G. V.; Wang, B.; Wang, S.; Ren, X. X.; Li, G. J.; Chen, W. H.; Liu, C. T.; Shen, C. Y. Polyzwitterionic cross-linked double network hydrogel electrolyte enabling high-stable Zn anode. *Nano Res.* **2024**, *17*, 5278–5287.
[54] Wang, X. L.; Lei, P. Y.; Zheng, C.; Wang, Z. S.; Wang, B.; Cui, X. D.; Cheng, J. L. Flexible and durable meter-long fiber-shaped Zn-ion battery enabled by zincophilic, tough double-network hydrogel electrolytes. *Adv. Funct. Mater.* **2025**, *35*, 2500916.
[55] Yang, Y. Q.; He, Q.; Hu, C.; Xie, X. F.; Liang, S. Q.; Zeng, Z. Y.; Fang, G. Z. Electron-initiated self-growth *in-situ* hydrogel electrolyte with gradient protection interface enables stable zinc metal batteries. *ACS Nano* **2025**, *19*, 21717–21728.
[56] Li, X. Y.; Jiang, Y.; Li, Y.; Wang, D. H.; Ran, F. Highly reversible zinc anode enabled by trehalose modified sodium alginate/carboxymethyl cellulose hydrogel electrolyte. *Chem. Eng. J.* **2025**, *509*, 161185.
[57] Zhang, Q. H.; Zhang, Y. X.; Ke, L. Z.; Jiang, H. N.; Huang, Y.; Nie, Z. X.; Jin, S. Y. Biocompatible hydrogel electrolyte with high ionic conductivity and transference number towards dendrite-free Zn anodes. *J. Mater. Sci. Technol.* **2025**, *225*, 40–48.
[58] Zhang, S. J.; Ao, H. S.; Dong, J. J.; Wang, D. D.; Wang, C. G.; Xu, X. J.; Hou, Z. G.; Yang, J. Dipole moment dictates the preferential immobilization in gel electrolytes for Ah-level aqueous zinc-metal batteries. *Angew. Chem., Int. Ed.* **2025**, *64*, e202414702.
[59] Xiao, X. M.; Ye, X. M.; Wu, Z. J.; Wu, X.; Yu, J. Z.; Gu, L.; Liu, S. Trace small molecular/nano-colloidal multiscale electrolyte additives enable ultra-long lifespan of zinc metal anodes. *Adv. Mater.* **2024**, *36*, 2408706.
[60] Tang, H.; Luo, H. Y.; Yu, G. T.; Wan, J. L.; Wu, L.; Chao, F. Y.; Zhang, W. W.; Cui, L. M.; Liu, Y.; Luo, P. et al. Modulating diffusion kinetics and interfacial stability via *in-situ* constructed self-healing interfaces for highly reversible zinc metal anodes. *Angew. Chem., Int. Ed.* **2025**, *64*, e202509622.
[61] Zhou, X. J.; Chen, Y. Z.; Zhen, F. X.; Wu, Y. B.; Li, W. P.; Yin, X. K.; Liu, L. M.; Ding, S. J.; Yu, W. Dual-shielding solvent strategy of high dipole-moment monomers for stabilizing gel polymer-based lithium metal batteries. *ACS Nano* **2025**, *19*, 14073–14084.
[62] Wei, W.; Zhang, M. H.; Yan, H.; Nan, S. B.; Cong, Z. X.; Dong, Y. F.; Tang, A. Simultaneous regulation of solvation shell and ion migration in morpholine-crosslinked polyacrylamide hydrogel electrolytes for durable zinc metal batteries. *J. Energy Chem.* **2025**, *102*, 703–711.
[63] Wang, L.; Guo, J. H.; Qi, Q.; Li, X. T.; Ge, Y. M.; Li, H. Y.; Chao, Y. F.; Du, J.; Cui, X. W. Revisiting dipole-induced fluorinated-anion decomposition reaction for promoting a LiF-rich interphase in lithium-metal batteries. *Nanomicro Lett.* **2025**, *17*, 111.